Sustainable Energy and Artificial Intelligence 1(1) (2025) 13-23 DOI: 10.61186/seai.2409-1006

Hamedan
University of Technology

Iranian Association of
Electrical and Electronics Engineers

Sustainable Energy and Artificial Intelligence

Online ISSN: 3060-8015

Journal Homepage: www.enai.hut.ac.ir

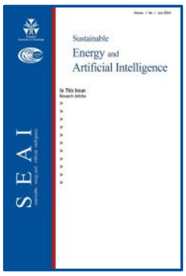

An Analytic 2D Subdomain Model for Slotless Electrical Machines with Internal Arc/Cubic Shape Permanent Magnets

Meisam Pourahmadi-Nakhli[1*], Seyed Hassan Daryanavard[1], Masoud Jokar-Kohanjani[2], Sina Soltani[3]

[1] *Department of Electrical and Computer Engineering, University of Hormozgan, Bandar Abbas, Iran*
[2] *Shiraz Electricity Distribution Company*
[3] *Department of Instrument and Control Engineering, Piramoon Pardazesh Qeshm, Tehran, Iran*
* *Corresponding Author:* m.pourahmadi@hormozgan.ac.ir

Article Info

Article type:
Original Article

Article history:
Received 2024-09-15;
Revised 2024-10-24;
Accepted 2024-11-17.

How to cite this article:
Pourahmadi-Nakhli, M., Daryanavard, S. H., Jokar Kouhanjani, M. and Soltani, S. (2025). An Analytic 2D Subdomain Model for Slotless Electrical Machines with Internal Arc/Cubic Shape Permanent Magnets. *Sustainable Energy and Artificial Intelligence*, *1*(1), 13-23.
DOI: 10.61186/seai.2409-1006

Abstract

Analytical modelling is a powerful tool for electrical machines design. Yet, subdomain arrangements and shapes inconsistent to the principal coordinate system of machine can pose a big challenge when developing an accurate analytical model. As PM arrangements and shapes in electrical motors are subject to change and optimization, this research focuses on developing an accurate 2-D analytical model for both cubic and arch – shaped PMs. To evaluate the accuracy of the model, a brushless electrical machine with spoke-hub PMs on the rotor is used to calculate the magnetic fields of the rotor and stator, as well as the resulting torque. However, comparison with Finite Element Method results indicates that for typical configurations involving cubic and arc-shaped PMs, the two-dimensional (2-D) analytic modeling can accurately compute electromagnetic quantities and the electromagnetic torque.

***Keywords*:** Subdomain Modelling; Rectangle Spoke PM; Arc-Shape Spoke PM; Finite Element Method.

1. Introduction

The subdomain analytic modeling of electric machines involves decomposing these systems into distinct components, allowing for targeted analytical solutions to electromagnetic equations. By focusing on individual regions—such as the stator, rotor, and air gap—this approach enables precise performance analysis and optimization. In comparison with huge computational burden of Finite Element Method (FEM), an analytic model for electromagnetic devices, when feasible, aids in the fast analysis, design, and computation of electromagnetic quantities. A substantial amount of literature exists regarding two-dimensional (2-D) analytic modeling of machines equipped with surface-mounted permanent magnets (PMs), as their unique geometries can be conveniently represented as sub-domains within polar coordinates. [1,2]. Regardless of the PM structure, finite element method is recognized as an accurate method for PM machine analysis [3-5]. Internal PMs machines have a variety of geometries like buried PMs [6-8], spoke PMs [9-16] and multi-layer PMs [17], many of which are too complex to be accurately approximated as 2-D sub-domains in a single coordinate system. Accordingly, the predominant body of literatures concerning the analysis and design of internal permanent magnet machines primarily utilizes numerical field calculation techniques, such as the Finite Element Method (FEM). [6-14]. Among different internal PMs structures, spoke-shape magnets can potentially be more accurately approximated as a polar sub-domain. In reference [15], the method of dividing the cubic spoke permanent magnet into multiple arc-shaped subdomains is employed to account for the influence of the rectangular spoke magnet in a two-dimensional air gap field analysis. However, a significant drawback of this method is the increase in the number of subdomains, which complicates the modeling process. Nevertheless, it is worth noting that manufacturers produce arc-shaped (pie slice-shaped) spoke configurations using either a single-piece magnet or a combination of several pieces. This paper aims to present a comprehensive two-dimensional analytical model for calculating the field of spoke-type internal permanent magnets, supplemented by hub-mounted magnets, all situated within an iron medium. The back electromotive force (back-EMF) is computed, and the torque is derived from the analysis of the Armature Reaction (AR) field distribution in conjunction with three-phase sinusoidal stator currents. The primary contribution of this developed model lies in its ability to accurately compute the electromagnetic parameters for both arc-shaped and cubic permanent magnet machines, achieving this with greater accuracy and reduced complexity compared to the approach outlined in [15]. The rest of the paper is as follows: Section 2 deals with assumptions needed for 2-D analytic modeling. Boundary conditions for developing the equations equal to knowns are explained in section 3. PM and current excitation Fourier series are identified in sections 4 and 5. Procedure of solving the general solutions and output calculations are in sections 6 to 9. The developed subdomain model is applied to an arc-shaped and a cubic spoke PM in sections 10 and 11, respectively. Sensitivity analysis of accuracy to parameters is dealt with in section 12, and concluding remarks in section 13.

2. ASSUMPTIONS

The following elements are taken into account for the development of the analytical model:

1. The spoke magnet segments are precisely defined in polar coordinates with tangential magnetization.
2. The permanent magnet spoke field is enhanced by hub-mounted magnets exhibiting radial magnetization around the shaft.
3. The magnetic flux density is generated solely in the radial and tangential directions, remaining independent of the z-axis.
4. The back-iron of both the stator and rotor is assumed to possess infinite permeability.
5. Effects related to end conditions and saturation are disregarded.
6. The stator configuration is designed to be slotless.
7. All regions are characterized by zero conductivity, leading to the exclusion of the eddy-current field.
8. The patterns of magnetization are independent of the radius. Applying the Maxwell's equations on the magnetic potential vector yields the following equation

$$\nabla^2 \boldsymbol{A} = -\mu_0\mu_r \boldsymbol{J} - \mu_0 \nabla \times \boldsymbol{M} \tag{1}$$

Where $\boldsymbol{A}$, $\boldsymbol{J}$ and $\boldsymbol{M}$ are magnetic potential vector, armature current density vector, and magnetization vector, respectively. In this investigation the problem includes four sub-domains with the Poisson's / Laplace's relationships as follows (see Fig. 1):

$$\nabla^2 \boldsymbol{A}^{\mathrm{w}} = -\mu_0 \boldsymbol{J} \tag{2}$$

$$\nabla^2 \boldsymbol{A}^{a} = \boldsymbol{0} \tag{3}$$

$$\nabla^2 \boldsymbol{A}^{\mathrm{m}_1} = -\mu_0 \nabla \times \boldsymbol{M}^{\mathrm{m}_1} \tag{4}$$

$$\nabla^2 \boldsymbol{A}^{\mathrm{m}_2} = -\mu_0 \nabla \times \boldsymbol{M}^{\mathrm{m}_2} \tag{5}$$

where $\mathrm{w}, a, \mathrm{m}_1$ and m_2 refer to the winding, gap, spoke magnet and hub magnet subdomains, respectively. For this problems, vectors are assumed to be in the following polar composition: $\boldsymbol{A} = [0,0,A_z(r,\theta)]$, $\boldsymbol{M} = [M_r(\theta), M_\theta(\theta), 0]$ and $\boldsymbol{J} = [0,0,J_z(\theta,t)]$.

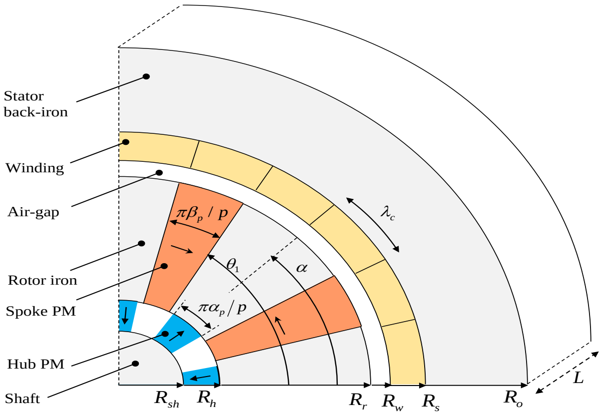

Fig. 1. Subdomains identified for the electric machine with Arc-shaped spoke and hub magnets

The magnetic flux density vector ($\boldsymbol{B}$) is derived by $\boldsymbol{B} = \nabla \times \boldsymbol{A}$ as

$$B_r(r,\theta) = \frac{1}{r}\frac{\partial A_z}{\partial \theta} \tag{6}$$

$$B_\theta(r,\theta) = -\frac{\partial A_z}{\partial r} \tag{7}$$

And, (2)-(5) can be rewritten as

$$\frac{\partial^2 A_z^w}{\partial r^2} + \frac{1}{r}\frac{\partial A_z^w}{\partial r} + \frac{1}{r^2}\frac{\partial^2 A_z^w}{\partial \theta^2} = -\mu_0 J_z \tag{8}$$

$$\frac{\partial^2 A_z^a}{\partial r^2} + \frac{1}{r}\frac{\partial A_z^a}{\partial r} + \frac{1}{r^2}\frac{\partial^2 A_z^a}{\partial \theta^2} = 0 \tag{9}$$

$$\frac{\partial^2 A_z^{m_1}}{\partial r^2} + \frac{1}{r}\frac{\partial A_z^{m_1}}{\partial r} + \frac{1}{r^2}\frac{\partial^2 A_z^{m_1}}{\partial \theta^2} = -\frac{\mu_0}{r}\left(M_\theta{}^{m_1} - \frac{\partial M_r{}^{m_1}}{\partial \theta}\right) \tag{10}$$

$$\frac{\partial^2 A_z^{m_2}}{\partial r^2} + \frac{1}{r}\frac{\partial A_z^{m_2}}{\partial r} + \frac{1}{r^2}\frac{\partial^2 A_z^{m_2}}{\partial \theta^2} = -\frac{\mu_0}{r}\left(M_\theta{}^{m_2} - \frac{\partial M_r{}^{m_2}}{\partial \theta}\right) \tag{11}$$

3. Boundary Conditions

The cross-sectional view of a slotless brushless machine with supposed spoke PMs and assisted by hub magnets is presented in Fig. 1.

Considering Fig. 1, boundary conditions that should be satisfied for this machine are

$$H_\theta^w(r,\theta)|_{r=R_s} = 0 \tag{12}$$

$$H_r^{m_1,k}(r,\theta)|_{(\theta=\theta_k)\&(\theta=\theta_k+\beta)} = 0 \tag{13}$$

$$H_\theta^{m_2}(r,\theta)|_{r=R_{sh}} = 0 \tag{14}$$

$$A_z^w(r,\theta)|_{r=R_w} = A_z^a(r,\theta)|_{r=R_w} \tag{15}$$

$$H_\theta^w(r,\theta)|_{r=R_w} = H_\theta^a(r,\theta)|_{r=R_w} \tag{16}$$

$$A_z^a(r,\theta)|_{r=R_r} = A_z^{m_1,k}(r,\theta)|_{r=R_r} \qquad \theta_k \le \theta \le \theta_k + \beta \tag{17}$$

$$H_\theta^a(r,\theta)|_{r=R_r} = \begin{cases} H_\theta^{m_1,k}(r,\theta)|_{r=R_r} & \theta \le \theta_k + \beta \\ 0 & \text{elsewhere} \end{cases} \tag{18}$$

$$A_z^{m_2}(r,\theta)|_{r=R_h} = A_z^{m_1,k}(r,\theta)|_{r=R_h} \qquad \theta_k \le \theta \le \theta_k + \beta \tag{19}$$

$$H_\theta^{m_2}(r,\theta)|_{r=R_h} = \begin{cases} H_\theta^{m_1,k}(r,\theta)|_{r=R_h} & \theta_k \le \theta \le \theta_k + \beta \\ 0 & \text{elsewhere} \end{cases} \tag{20}$$

where $k = 1, \ldots, 2p$ is the index of each spoke magnet, $\beta = \pi\beta_p/p$ is the span angle of spoke PM arc (β_p is the spoke PM span per pole pitch) θ_k is the first edge angle of k^{th} spoke magnet from stator reference and p is the number of pole pairs.

4. Magnetization Vector

In the case of 2-D polar subdomains, the magnetization can be written as

$$\boldsymbol{M} = M_r\boldsymbol{r} + M_\theta\boldsymbol{\theta} \tag{21}$$

where $\boldsymbol{r}$ and $\boldsymbol{\theta}$ are the unit vectors in polar coordinate. In order to facilitate the analytical solution of the partial differential equations, it is common to represent the radial and tangential parts of magnetization patterns with Fourier series expansion as

$$M_r(\theta) = \sum_{\frac{n}{p}=1,3,5,\ldots}^{\infty} M_{rn}cos(n\theta - n\alpha) \tag{22}$$

$$M_\theta(\theta) = \sum_{\frac{n}{p}=1,3,5,\ldots}^{\infty} M_{\theta n}sin(n\theta - n\alpha) \tag{23}$$

where M_{rn} and $M_{\theta n}$ are respectively the n^{th}harmonics of the radial and tangential magnetizations in the Fourier series and $\alpha = \omega t + \alpha_0$ is rotor angular position with respect to the stator reference as shown in Fig. 1. α_0 is the initial position and ω is the angular velocity of rotor. For magnetization in the hub magnet, it is convenient to state the whole hub region by a single magnetization as

$$M_r^{m_2}(\theta) = \sum_{\frac{u}{p}=1,3,5,\ldots}^{\infty} M_{ru}^{m_2}cos(u\theta - u\alpha) \tag{24}$$

$$M_\theta^{m_2}(\theta) = \sum_{\frac{u}{p}=1,3,5,\ldots}^{\infty} M_{\theta u}^{m_2}sin(u\theta - u\alpha) \tag{25}$$

where for assumed radial magnetization pattern

$$M_{ru}^{m_2} = \frac{4pB_{rem}^{m_2}}{\mu_0 u\pi}sin\left(\frac{u\pi\alpha_p}{2p}\right) \tag{26}$$

$$M_{\theta u}^{m_2} = 0 \tag{27}$$

and α_p is the hub magnet arc per pole pitch ratio. Herein, the magnetization of each spoke magnet is assumed to have only constant tangential component. In this condition, representation of the magnetization vector in terms of Fourier series makes the general solution difficult to satisfy the boundary condition of (13). Accordingly, the problem is solved easier by presenting the magnetization of k^{th} spoke magnet via constant values as

$$M_r^{m_1,k}(\theta) = 0 \tag{28}$$

$$M_\theta^{m_1,k}(\theta) = (-1)^k M_{0\theta}^{m_1} \tag{29}$$

$$M_{0\theta}^{m_1} = B_{rem}^{m1}/\mu_0 \tag{30}$$

where $B_{rem}^{m1}$is the remanence flux density of the spoke magnet.

5. Armature Current Distribution

The spatial distribution of current in a slotless machine with a q-phase balanced winding can be presented as [29].

$$J(\theta,t)=\sum_{v=1}^{\infty}J_v^s(t)\sin(v\theta)+J_v^c(t)\cos(v\theta) \quad (31)$$

where

$$J_v^s(t)=\sum_{j=1}^{q}\frac{4pN_t}{\pi|R_s^2-R_w^2|}k_{pv}k_{dv}i_j(t)\cos(v\delta_j) \quad (32)$$

$$J_v^c(t)=-\sum_{j=1}^{q}\frac{4pN_t}{\pi|R_s^2-R_w^2|}k_{pv}k_{dv}i_j(t)\sin(v\delta_j) \quad (33)$$

N_t is the number of turns per pole in each phase, k_{pv} is pitch factor of windings, k_{dv} is distribution factor, $i_j(t)$ is temporal current and δ_j is the shift of the phase j.

6. General Solution

The general solutions serving Equations (8)-(11) are in the following form

$$A_z^w(r,\theta)=a_0^w+\sum_{v=1,2,3,\dots,V}(a_v^w r^v+b_v^w r^{-v}+k_v^{sw}r^2)sin(v\theta)+(c_v^w r^v+d_v^w r^{-v}+k_v^{cw}r^2)cos(v\theta) \quad (34)$$

$$A_z^a(r,\theta)=a_0^a+\sum_{v=1,2,3,\dots,V}(a_v^a r^v+b_v^a r^{-v})sin(v\theta)+(c_v^a r^v+d_v^a r^{-v})cos(v\theta) \quad (35)$$

For k^{th} spoke magnet where $k=1,2,\dots,2p$

$$A_z^{m_1,k}(r,\theta)=\left\{a_0^{m_1,k}+b_0^{m_1,k}lnr+\sum_{n=1,2,3,\dots,N}\left(a_n^{m_1,k}r^{n\pi/\beta}+b_n^{m_1,k}r^{-n\pi/\beta}\right)cos\left(\frac{n\pi}{\beta}(\theta-\theta_k)\right)\right\}+A_{z_p}^{m_1,k} \quad (36)$$

$$A_z^{m_2}(r,\theta)=a_0^{m_2}+\sum_{u=1,2,3,\dots,U}\left(a_u^{m_2}r^u+b_u^{m_2}r^{-u}+k_u^{m_2}\right)sin(u\alpha)cos(u\theta)+\left(c_u^{m_2}r^u+d_u^{m_2}r^{-u}-k_u^{m_2}\right)cos(u\alpha)sin(u\theta) \quad (37)$$

where

$$A_{z_p}^{m_1,k}=k_p^{m_1,k}r=-\mu_0 M_\theta^{m_1,k}r \quad (38)$$

$$k_u^{m_2}=\begin{cases}\mu_0\dfrac{uM_{ru}^{m_2}+M_{\theta u}^{m_2}}{u^2-1} & u\neq 1\\ -\mu_0\dfrac{M_{ru}^{m_2}+M_{\theta u}^{m_2}}{2}lnr & u=1\end{cases} \quad (39)$$

$$k_v^{sw}=\begin{cases}\dfrac{\mu_0 J_v^s}{v^2-4} & v\neq 2\\ -\dfrac{\mu_0 J_v^s}{4}lnr & v=2\end{cases} \quad (40)$$

$$k_v^{cw}=\begin{cases}\dfrac{\mu_0 J_v^c}{v^2-4} & v\neq 2\\ -\dfrac{\mu_0 J_v^c}{4}lnr & v=2\end{cases} \quad (41)$$

and V,N,U are the maximum harmonic number assumed for the corresponding accurate solution.

7. Integral Constant

In order to complete the general solutions, the integral constants need to be identified. Herein, PM and AR excitations are modeled simultaneously to establish a more abstract and convenient relationship.

Incorporating the general solutions stated respectively by (34), (36) and (37) to the boundary conditions (12), (13) and (14) leads to the following expressions

$$A_z^w(r,\theta)=a_0^w+\sum_{v=1}^{V}r\left\{\hat{b}_v^w\left[\left(\frac{R_r}{R_s}\right)^{v+1}\left(\frac{r}{R_s}\right)^{v-1}+\left(\frac{R_r}{r}\right)^{v+1}\right]-\zeta_{v1}^s\left(\frac{r}{R_s}\right)^{v-1}+k_v^{sw}r\right\}\sin(v\theta)+r\left\{\hat{d}_v^w\left[\left(\frac{R_r}{R_s}\right)^{v+1}\left(\frac{r}{R_s}\right)^{v-1}+\left(\frac{R_r}{r}\right)^{v+1}\right]-\zeta_{v1}^c\left(\frac{r}{R_s}\right)^{v-1}+k_v^{cw}r\right\}\cos(v\theta) \quad (42)$$

$$k_u^{m_2}=\begin{cases}\mu_0\dfrac{uM_{ru}^{m_2}+M_{\theta u}^{m_2}}{u^2-1} & u\neq 1\\ -\mu_0\dfrac{M_{ru}^{m_2}+M_{\theta u}^{m_2}}{2}lnr & u=1\end{cases} \quad (43)$$

$$A_z^{m_2}(r,\theta)=\sum_{u=1}^{U}r\left\{\left[\left(\frac{r}{R_h}\right)^{u-1}+\left(\frac{R_{sh}}{R_h}\right)^{u-1}\left(\frac{R_{sh}}{r}\right)^{u+1}\right]\hat{a}_u^{m_2}-\zeta_u^{m_2}\left(\frac{R_{sh}}{r}\right)^{u+1}-k_u^{m_2}\right\}\sin(u\alpha)\cos(u\theta)+r\left\{\left[\left(\frac{r}{R_h}\right)^{u-1}+\left(\frac{R_{sh}}{R_h}\right)^{u-1}\left(\frac{R_{sh}}{r}\right)^{u+1}\right]\hat{c}_u^{m_2}+\zeta_u^{m_2}\left(\frac{R_{sh}}{r}\right)^{u+1}+k_u^{m_2}\right\}\cos(u\alpha)\sin(u\theta) \quad (44)$$

where

$$\zeta_{v1}^s=\frac{R_s\mu_0 J_v^s}{v}\begin{cases}\dfrac{2}{v^2-4} & v\neq 2\\ -\dfrac{2\ln R_s+1}{4} & v=2\end{cases} \quad (45)$$

$$\zeta_{v1}^c=\frac{R_s\mu_0 J_v^c}{v}\begin{cases}\dfrac{2}{v^2-4} & v\neq 2\\ -\dfrac{2\ln R_s+1}{4} & v=2\end{cases} \quad (46)$$

$$\zeta_u^{m_2} = \mu_0 \begin{cases} \dfrac{M_{ru}^{m_2} + uM_{\theta u}^{m_2}}{u^2 - 1} & u \neq 1 \\ -\dfrac{M_{ru}^{m_2} + M_{\theta u}^{m_2}}{2}(1 + \ln(R_{sh})) + M_{\theta u}^{m_2} & u = 1 \end{cases} \tag{47}$$

Considering the continuity conditions at the gap - winding boundary, i.e., (15) and (16), the general solution of air gap is achieved by doing some algebraic manipulations as well as substituting the equal terms.

$$\begin{aligned} A_z^a(r,\theta) &= a_0^w \\ &+ \sum_{v=1}^{V} r\left\{\hat{b}_v^w\left[\left(\frac{R_r}{R_s}\right)^{v+1}\left(\frac{r}{R_s}\right)^{v-1} + \left(\frac{R_r}{r}\right)^{v+1}\right]\right. \\ &- \zeta_{v1}^s\left(\frac{r}{R_s}\right)^{v-1} + \frac{\zeta_{v2}^s + \zeta_{v3}^s}{2}\left(\frac{r}{R_w}\right)^{v-1} \\ &+ \left.\frac{\zeta_{v2}^s - \zeta_{v3}^s}{2}\left(\frac{R_w}{r}\right)^{v+1}\right\}\sin(v\theta) \\ &+ r\left\{\hat{d}_v^w\left[\left(\frac{R_r}{R_s}\right)^{v+1}\left(\frac{r}{R_s}\right)^{v-1} + \left(\frac{R_r}{r}\right)^{v+1}\right]\right. \\ &- \zeta_{v1}^c\left(\frac{r}{R_s}\right)^{v-1} + \frac{\zeta_{v2}^c + \zeta_{v3}^c}{2}\left(\frac{r}{R_w}\right)^{v-1} \\ &+ \left.\frac{\zeta_{v2}^c - \zeta_{v3}^c}{2}\left(\frac{R_w}{r}\right)^{v+1}\right\}\cos(v\theta) \end{aligned} \tag{48}$$

where

$$\zeta_{v2}^s = R_a\mu_0 J_v^s \begin{cases} \dfrac{1}{v^2 - 4} & v \neq 2 \\ -\dfrac{2\ln R_a}{4} & v = 2 \end{cases} \tag{49}$$

$$\zeta_{v2}^c = R_a\mu_0 J_v^c \begin{cases} \dfrac{1}{v^2 - 4} & v \neq 2 \\ -\dfrac{2\ln R_a}{4} & v = 2 \end{cases} \tag{50}$$

$$\zeta_{v3}^s = \frac{R_a\mu_0 J_v^s}{v} \begin{cases} \dfrac{2}{v^2 - 4} & v \neq 2 \\ -\dfrac{2\ln R_a + 1}{4} & v = 2 \end{cases} \tag{51}$$

$$\zeta_{v3}^c = \frac{R_a\mu_0 J_v^c}{v} \begin{cases} \dfrac{2}{v^2 - 4} & v \neq 2 \\ -\dfrac{2\ln R_a + 1}{4} & v = 2 \end{cases} \tag{52}$$

Now there are nine sets of integral constants to be known including $a_0^w, \hat{b}_v^w, \hat{d}_v^w, a_0^{m_1,k}, b_0^{m_1,k}, \hat{a}_n^{m_1,k}, \hat{b}_n^{m_1,k}, \hat{a}_u^{m_2}$ and $\hat{b}_u^{m_2}$.

Taking the average of both sides of (17) over $[\theta_k, \theta_k + \beta]$ as

$$\frac{1}{\beta}\int_{\theta_k}^{\theta_k+\beta} A_z^a(R_r,\theta)d\theta = \frac{1}{\beta}\int_{\theta_k}^{\theta_k+\beta} A_z^{m_1,k}(R_r,\theta)d\theta \tag{53}$$

yields the $2p$ equations, equivalent to the combination of the first row of (62).

By taking the correlation of (17) to $\cos(n\pi/\beta(\theta - \theta_k))$ over $[\theta_k, \theta_k + \beta]$ as

$$\begin{aligned} &\frac{2}{\beta}\int_{\theta_k}^{\theta_k+\beta} A_z^a(R_r,\theta)\cos\left(\frac{n\pi}{\beta}(\theta - \theta_k)\right)d\theta \\ &= \frac{2}{\beta}\int_{\theta_k}^{\theta_k+\beta} A_z^{m_1,k}(R_r,\theta)\cos\left(\frac{n\pi}{\beta}(\theta - \theta_k)\right)d\theta \end{aligned} \tag{54}$$

yields the $2pN$ equations, equivalent to the combination of the second row of (62).

Correlation of (18) to $\cos(v\theta)$ over $[0,2\pi]$ as

$$\begin{aligned} &\frac{1}{\pi}\int_0^{2\pi} H_\theta^a(R_r,\theta)\cos(v\theta)d\theta \\ &= \frac{1}{\pi}\sum_{k=1}^{2p}\int_{\theta_k}^{\theta_k+\beta} H_\theta^{m_1,k}(R_r,\theta)\cos(v\theta)d\theta \end{aligned} \tag{55}$$

gives the V equations, equivalent to the combination of the fifth row of (62).

Similarly, correlation of (18) to $\sin(v\theta)$ in the same way as

$$\begin{aligned} &\frac{1}{\pi}\int_0^{2\pi} H_\theta^a(R_r,\theta)\sin(v\theta)d\theta \\ &= \frac{1}{\pi}\sum_{k=1}^{2p}\int_{\theta_k}^{\theta_k+\beta} H_\theta^{m_1,k}(R_r,\theta)\sin(v\theta)d\theta \end{aligned} \tag{56}$$

results in the V equations, equivalent to the combination of the sixth row of (62).

Taking the average of both sides of (19) as

$$\frac{1}{\beta}\int_{\theta_k}^{\theta_k+\beta} A_z^{m_1,k}(R_h,\theta)d\theta = \frac{1}{\beta}\int_{\theta_k}^{\theta_k+\beta} A_z^{m_2}(R_h,\theta)d\theta \tag{57}$$

converts it to the $2p$ equations, equivalent to the combination of the third row of (62).

By Correlating (19) to $\cos\left(n\pi/\beta(\theta - \theta_k)\right)$ over $[0,2\pi]$ as

$$\begin{aligned} &\frac{2}{\beta}\int_{\theta_k}^{\theta_k+\beta} A_z^{m_2}(R_h,\theta)\cos\left(\frac{n\pi}{\beta}(\theta - \theta_k)\right)d\theta \\ &= \frac{2}{\beta}\int_{\theta_k}^{\theta_k+\beta} A_z^{m_1,k}(R_h,\theta)\cos\left(\frac{n\pi}{\beta}(\theta - \theta_k)\right)d\theta \end{aligned} \tag{58}$$

the $2pN$ equations, equivalent to the combination of the forth row of (62) is gained.

Correlation of (20) to $\sin(v\theta)$ over $[0,2\pi]$ as

$$\begin{aligned} &\frac{1}{\pi}\int_0^{2\pi} H_\theta^{m_2}(R_h,\theta)\sin(v\theta)d\theta \\ &= \frac{1}{\pi}\sum_{k=1}^{2p}\int_{\theta_k}^{\theta_k+\beta} H_\theta^{m_1,k}(R_h,\theta)\sin(v\theta)d\theta \end{aligned} \tag{59}$$

gives the U equations, equivalent to the combination of the eighth row of (62).

Correlating both sides of (20) to $\cos(v\theta)$ over $[0,2\pi]$ as

$$\frac{1}{\pi}\int_0^{2\pi} H_\theta^{m_2}(R_h,\theta)\sin(v\theta)d\theta \tag{60}$$

$$= \frac{1}{\pi}\sum_{k=1}^{2p}\int_{\theta_k}^{\theta_k+\beta} H_\theta^{m_1,k}(R_h,\theta)\sin(v\theta)d\theta$$

results in the following U equations, equivalent to the combination of the seventh row of (62).

Taking the average of both sides of (20) as

$$\frac{1}{\pi}\sum_{k=1}^{2p}\int_{\theta_k}^{\theta_k+\beta} H_\theta^{m_1,k}(R_h,\theta)d\theta = \frac{1}{\pi}\int_0^{2\pi} H_\theta^{m_2}(R_h,\theta)d\theta \tag{61}$$

over [0,2π] yields $2p$ equations, equivalent to the combination of the ninth row of (62).

By rearranging (53)-(61) as linear combinations of integral coefficients and separating the excitation-related terms, the following linear matrix equation is established

$$\begin{bmatrix} \Lambda^{11} & \Lambda^{12} & \Lambda^{13} & \Lambda^{14} & \Lambda^{15} & \mathbf{0} & \mathbf{0} & \mathbf{0} & \mathbf{0} \\ \mathbf{0} & \Lambda^{22} & \Lambda^{23} & \mathbf{0} & \mathbf{0} & \Lambda^{26} & \Lambda^{27} & \mathbf{0} & \mathbf{0} \\ \mathbf{0} & \mathbf{0} & \mathbf{0} & \Lambda^{34} & \Lambda^{35} & \mathbf{0} & \mathbf{0} & \Lambda^{38} & \Lambda^{39} \\ \mathbf{0} & \mathbf{0} & \mathbf{0} & \mathbf{0} & \mathbf{0} & \Lambda^{46} & \Lambda^{47} & \Lambda^{48} & \Lambda^{49} \\ \mathbf{0} & \mathbf{0} & \Lambda^{53} & \mathbf{0} & \Lambda^{55} & \Lambda^{56} & \Lambda^{57} & \mathbf{0} & \mathbf{0} \\ \mathbf{0} & \Lambda^{62} & \mathbf{0} & \mathbf{0} & \Lambda^{65} & \Lambda^{66} & \Lambda^{67} & \mathbf{0} & \mathbf{0} \\ \mathbf{0} & \mathbf{0} & \mathbf{0} & \mathbf{0} & \Lambda^{75} & \Lambda^{76} & \Lambda^{77} & \Lambda^{78} & \mathbf{0} \\ \mathbf{0} & \mathbf{0} & \mathbf{0} & \mathbf{0} & \Lambda^{85} & \Lambda^{86} & \Lambda^{87} & \mathbf{0} & \Lambda^{89} \\ \mathbf{0} & \mathbf{0} & \mathbf{0} & \mathbf{0} & \Lambda^{95} & \mathbf{0} & \mathbf{0} & \mathbf{0} & \mathbf{0} \end{bmatrix} \begin{bmatrix} a_0^w \\ \boldsymbol{b}^w \\ \boldsymbol{d}^w \\ \boldsymbol{a}_0^{m_1} \\ \boldsymbol{b}_0^{m_1} \\ \boldsymbol{a}^{m_1} \\ \boldsymbol{b}^{m_1} \\ \boldsymbol{a}^{m_2} \\ \boldsymbol{c}^{m_2} \end{bmatrix} = \begin{bmatrix} \Gamma^{1,PM1} \\ \mathbf{0} \\ \Gamma^{3,PM1} \\ \Gamma^{4,PM1} \\ \mathbf{0} \\ \mathbf{0} \\ \Gamma^{7,PM2} \\ \Gamma^{8,PM2} \\ \mathbf{0} \end{bmatrix} + \begin{bmatrix} \Gamma^{1,AR} \\ \Gamma^{2,AR} \\ \mathbf{0} \\ \mathbf{0} \\ \Gamma^{5,AR} \\ \Gamma^{6,AR} \\ \mathbf{0} \\ \mathbf{0} \\ \mathbf{0} \end{bmatrix} \tag{62}$$

By calculation of the integral coefficients, the components of the magnetic quantities of subdomains are obtained.

8. Instantaneous Torque Calculation

The instantaneous torque at each angular position can be obtained from the Maxwell stress tensor as

$$\begin{aligned} T(\alpha) &= L\int_{-\pi}^{\pi}\frac{1}{\mu_0}\Big(B_{r,PM}^a(R_a,\theta') \\ &+ B_{r,AM}^a(R_a,\theta')\Big)\Big(B_{\theta,PM}^a(R_a,\theta') \\ &+ B_{\theta,AM}^a(R_a,\theta')\Big)R_a{}^2 d\theta' \end{aligned} \tag{63}$$

where L is the axial length of machine, $B_{r,PM}^a$ and $B_{\theta,PM}^a$ are the radial and tangential vectors of the air-gap flux density produced by PM at $R_a = (R_w + R_r)/2$. While $B_{r,AM}^a$ and $B_{\theta,AM}^a$ are radial and tangential parts of the air-gap flux density resulted by AR. θ' serves as a dummy variable for integration. The extended integral of (63) is

$$\begin{aligned} T(\alpha) &= \frac{LR_a^2}{\mu_0}\int_{-\pi}^{\pi}\big(B_{r,PM}^a B_{\theta,PM}^a + B_{r,AR}^a B_{\theta,PM}^a \\ &+ B_{r,PM}^a B_{\theta,AR}^a + B_{r,AR}^a B_{\theta,AR}^a\big)_{|(r=R_a \& \,\theta=\theta')}\ d\theta' \end{aligned} \tag{64}$$

9. Back-Emf Calculation

The back–EMF of windings are calculated by magnetic flux linked to each coil. For a q-phase stator winding, the full flux linked to the k^{th} coil in the j^{th} phase is

$$\emptyset_{j,k}(\alpha) = R_W L\int_{-\frac{\theta_c}{2p}+\delta_{j,k}}^{\frac{\theta_c}{2p}+\delta_{j,k}} B_r^w(R_W,\theta'-\alpha)d\theta' \tag{65}$$

where $j = 1,2,\ldots q$, $k = 1,2,\ldots N_{cp}$, N_{cp} is the number of coils of phase j , $R_W = (R_w + R_s)/2$ is the average radius, at which point the winding is assumed to be lumped, and $\delta_{j,k} = 2\pi(k-1)/p + 2\pi(j-1)/pq$. Having series coils, the back-EMF in phase j is

$$E_j = -N_t\omega\sum_{k=1}^{N_{cp}}\frac{d\emptyset_{j,k}}{d\alpha} \tag{66}$$

In this way, from analytic solution of flux densities of the spoke machine, the back-EMF generated is

$$\begin{aligned} E_j(\alpha) &= -2N_t\,\omega R_W L\sum_{k=1}^{N_{cp}}\sum_{v=1,2,\ldots}^{\infty} v\left(\left(\frac{R_r}{R_s}\right)^{v+1}\left(\frac{R_W}{R_s}\right)^{v-1} \right. \\ &\left. + \left(\frac{R_r}{R_W}\right)^{v+1}\right)\sin\left(\frac{v\theta_c}{2p}\right)\Big(\hat{b}_v^w\sin\big(v(\delta_{j,k}-\alpha)\big) \\ &+ \hat{d}_v^w\cos\big(v(\delta_{j,k}-\alpha)\big)\Big) \end{aligned} \tag{67}$$

10. Arc-Shaped Spoke PM Case Study

A motor featuring internal spoke permanent magnets supported by hub-embedded magnets has been analyzed to determine the distribution of magnetic flux density in the middle of air gap. The detail characteristic of this machine referring to Fig. 1 is presented in table 1.

The results obtained from analytical calculations are compared with those obtained from finite element method (FEM) simulations of the case with the same characteristics. FEM is renowned for its ability to deliver highly detailed and accurate results, particularly when dealing with complex geometries and non-linear material behaviors, yet it demands substantial computational resources and specialized expertise. Conversely, analytical methods provide a more expedient approach, allowing for rapid estimations and straightforward implementation, although they are often constrained by simplifications that may compromise accuracy in intricate designs. In this study for both the analytical and FEM analyses, the relative permeability of iron is assumed to be infinite by utilizing a significantly large value.

Table 1. Arc Shaped Spoke PM Machine Parameters

Variables	Unit	Values
q	-	3
p	-	3
β_p	-	0.3
α_p	-	0.7
$\mu_{r_{m1}},\ \mu_{r_{m2}}$	-	1.045
$B_{rem}^{m1}, B_{rem}^{m2}$	(T)	1.1
I_m	(A)	10
P_r	(kW)	2
R_{sh}	(mm)	10
R_h	(mm)	20
R_r	(mm)	60
R_w	(mm)	65
R_s	(mm)	70
L	(mm)	15
ω	(rad/s)	160
A_c	(mm^2)	2
λ_c	(rad)	π/pq
$\theta_c = \theta_p$	$(electrical\ rad)$	π
N, U, V	-	100

For accuracy evaluation of the analytic model, the spoke-type PM motor specifications are considered near to an actual motor (table 1).

Fig. 2 shows the radial and tangential components of distributed PM-produced flux density in the middle of air gap. Obviously, simulation results of analytical model are in good match with those of FEM. Assisting effect of hub magnets in magnifying radial flux is also evident. Here sinusoidal currents are applied and their magnetic flux density has been calculated first considering PMs without any magnetization. Similarly, the PM-originated magnetic flux distribution is calculated in absence of armature reaction. Fig. 2 indicates the PM generated radial and tangential values of the air-gap flux density at $\alpha = 0$ electrical degree only due to the spoke magnets with hub magnet and without it. The assisting role of hub magnet in field amplification is evident. Similarly, Fig. 3a shows the same components of the flux density only due to AR. Fig. 3b shows the same fields at α = 90 electrical degrees. It is important to note that AR flux distribution is sensitive to rotor position α, and that is because the saliency of the spoked-rotor significantly influences the magnetic reluctance of AR when rotor position changes.

By comparing analytical results to numerical ones in all figures, the high accuracy of the analytic model is evident.

Fig. 4 depicts the resultant instantaneous torque due to the PMs and AR excitations. The amplifying effect of the hub magnet in instantaneous torque is shown in Fig. 4. Also, analytic calculation of instantaneous torque satisfactorily agrees with the results of FEM analysis.

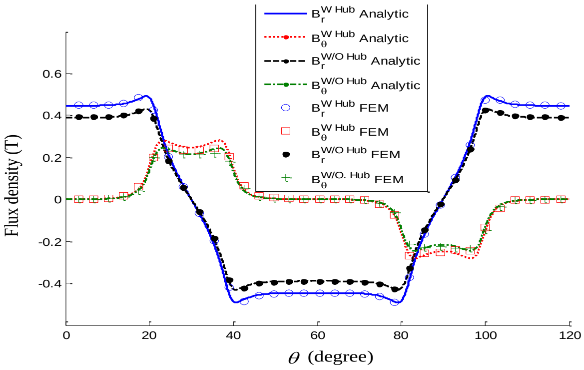

Fig 2. The PM generated radial and tangential values of the air-gap flux density when α = 0 with (W) hub and without (W/O) hub magnet

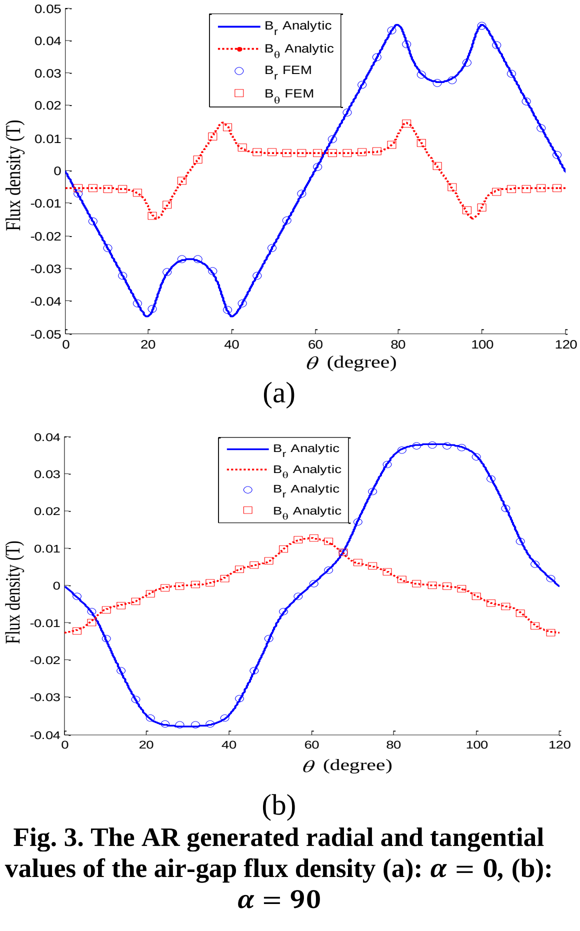

Fig. 3. The AR generated radial and tangential values of the air-gap flux density (a): $\alpha = 0$, (b): $\alpha = 90$

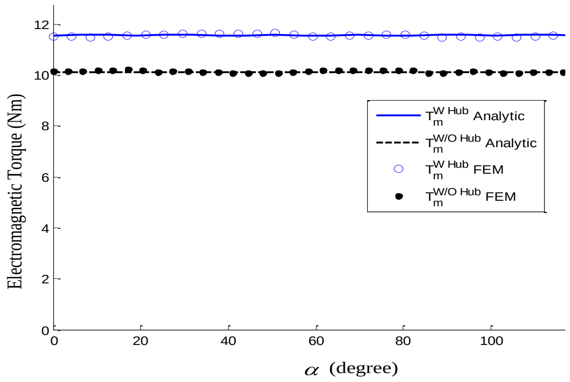

Fig. 4. The Electromagnetic Torque

The first phase back-EMF due to spoke magnets with and without hub magnets is shown in Fig. 5 and compared to those of FEM results. There is a little mismatch between the FEM and analytic results at knee points of back-EMF. This is due to different radii at which analytical and FEM approaches calculate the back-EMF. In analytic model we assumed the winding coils are lumped at the middle of the winding region (R_W) while FEM integrates the back-EMF distributed between R_w and R_s.

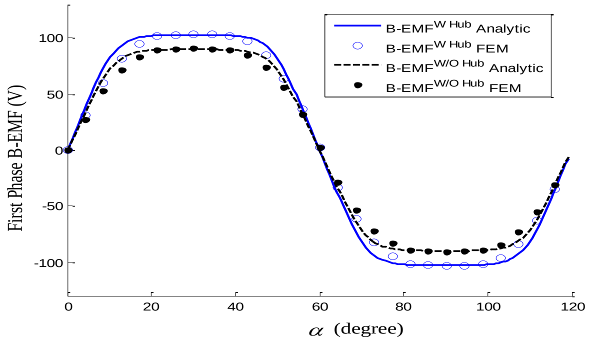

Fig. 5. The phase back-EMF waveform for both analytic and F

11. Cubic Spoke PM Case Study

Many of PM pieces are manufactured in cubic shape for their convenient fabrication and the economical process of core press punch. On this basis it is important to evaluated the accuracy of the model on such electric machines with cubic PMs. In order to represent the rectangular cross section of the cubic spoke magnet depicted in Fig. 6 using an arc-shaped area, it is assumed that the average thickness of the arc corresponds to the thickness of the cubic spoke permanent magnet (PM). Additionally, it is presumed that the arc-shaped PM maintains the same depth as the cubic spoke. For the cubic hub magnets, the approximation is based on the assumption that the cross-sectional area remains consistent under the same PM thickness. The parameters of the cubic spoke PM machine under investigation are detailed in Table 2. The simulation results for the approximate two-dimensional analytical model of the cubic PM spoke machine, alongside its precise finite element method (FEM) results, are illustrated in Fig. 7 through 10. The findings indicate that the approximate two-dimensional analytical model is capable of estimating the magnetic quantities with a satisfactory level of accuracy.

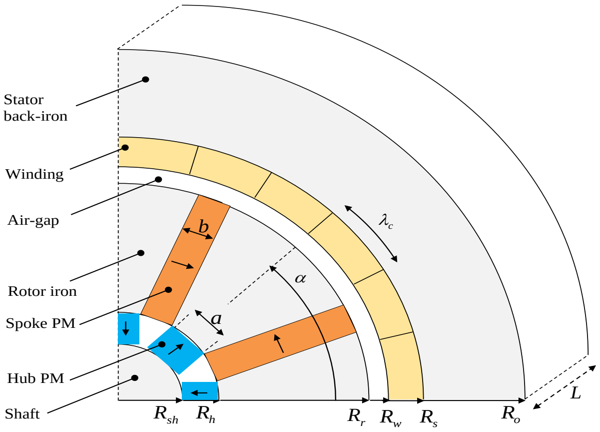

Fig. 6. PMs machine with cubic magnets

There exists a discrepancy in the estimation of tangential flux densities (refer to figure 8), as the influence of the spoke thickness at the outer rotor radii is more significant on the tangential flux pathway compared to the radial pathway. This variation is also reflected in the calculations of electromagnetic torque presented in Fig. 9. The evident mismatch in Fig. 9 is due to the flux mismatches around the spike regions, and the fact that electromagnetic torque is proportional to PM and AR fluxes. Furthermore, Fig. 10 demonstrates a high level of accuracy in the estimation of back electromotive force (back-EMF).

Table 2. Cubic Spoke PM Machine Parameters

Variables	Unit	Values
q	-	3
p	-	3
b	mm	12
a	mm	10
$\mu_{r_{m1}},\quad \mu_{r_{m2}}$	-	1.045
$B_{rem}^{m1}, B_{rem}^{m2}$	(T)	1.1
I_m	(A)	10
P_r	(kW)	2
R_{sh}	(mm)	10
R_h	(mm)	20
R_r	(mm)	60
R_w	(mm)	65
R_s	(mm)	70
L	(mm)	15
ω_r	(rad/s)	160
A_c	(mm^2)	2
λ_c	(rad)	π/pq
$\theta_c = \theta_p$	$(electrical\ rad)$	π
N, U, V	-	100

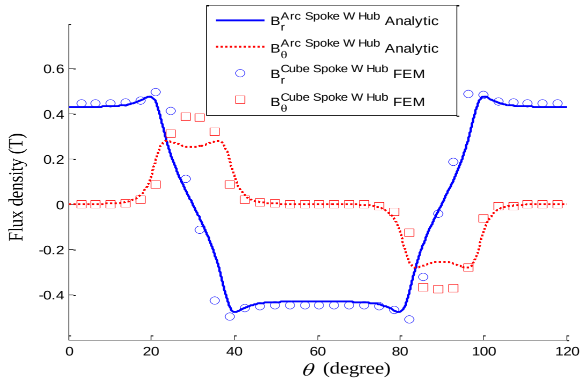

Fig. 7. The PM generated radial and tangential values of the air-gap flux density when α = 0 with (W) hub and without (W/O) hub magnet

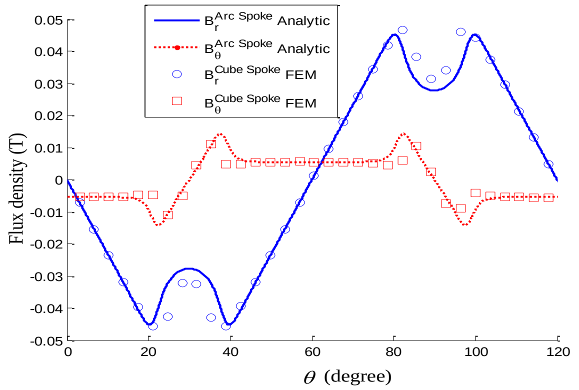

(a)

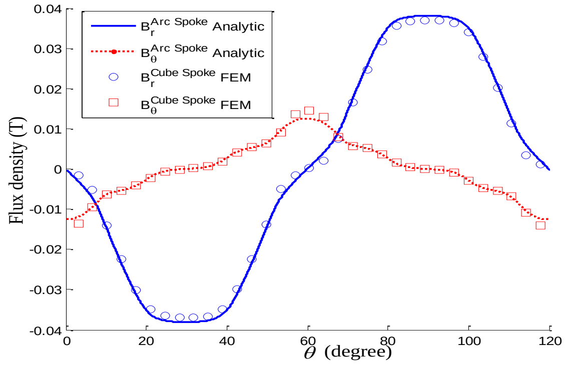

(b)

Fig. 8. The AR generated radial and tangential values of the air-gap flux density (a): $\alpha = 0$, (b): $\alpha = 90$

In order to better evaluate the results of the proposed method, the root mean square error index in the calculations of different quantities is calculated in the following form.

$$\mathrm{NRMSE} = \sqrt{\frac{\sum_i (q_{ANA}(i) - q_{FEM}(i))^2}{\sum_i q_{FEM}(i)^2}} \qquad (68)$$

Where $q_{ANA}(i)$ and $q_{FEM}(i)$ are the values of quantities obtained by analytical method and FEM, respectively. The NRMSE index expresses the error ratio to the value obtained from the finite element method.

Table 3 shows the relative error values of the two-dimensional analysis model in the estimation of machine quantities with arc-shaped and rectangular magnets.

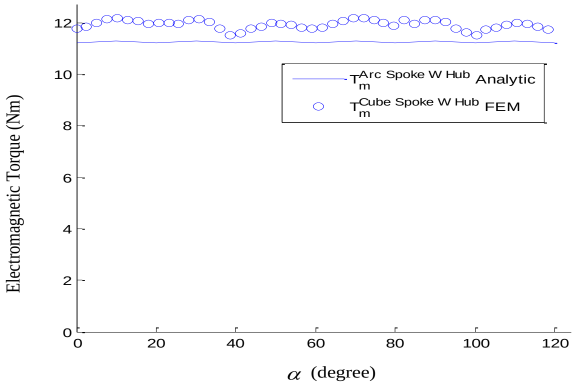

Fig. 9. The Electromagnetic Torque

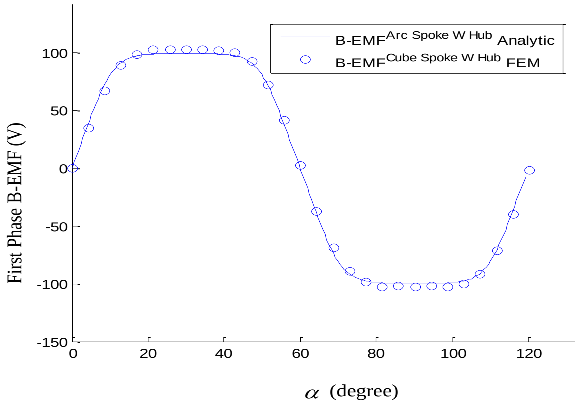

Fig. 10. The first phase Back-EMF

Table 3. NRMSE of the results

Quantity	Excitation	$\boldsymbol{\alpha}$ (Degree)	**NRMSE**	
			Cubic PM	ARC PM
$B_r^a(R_a,\theta)$	PM	0	0.110	0.003
$B_\theta^a(R_a,\theta)$	PM	0	0.382	0.009
$B_r^a(R_a,\theta)$	PM	90	0.151	0.004
$B_\theta^a(R_a,\theta)$	PM	90	0.443	0.005
$B_r^a(R_a,\theta)$	AR	0	0.101	0.002
$B_\theta^a(R_a,\theta)$	AR	0	0.103	0.003
$BEMF$	AR	0 to 360	0.046	0.091
T_m	AR&PM	0 to 360	0.134	0.010

12. Sensitivity Analysis

Results suggest that inconsistent shape of cubic PMs, especially spoke ones, to polar coordinate of the rest subdomains is the cause of higher NRMSEs in the cubic case. Accordingly, this section is devoted to examine how the accuracy of the analytical model is sensitive to inconsistent parameters of the cubic PM. For this purpose, the spoke thickness (b) and spoke depth ($R_r - R_h$) are subject to change. Figs. 11 and 12 show the NRMSE change for the calculated torque under variations of spoke dimensions around their initial values. It is important to note that under such variations air gap and other radial thicknesses of rotor and stator remained unchanged. For each scenario, NRMSE of the result samples of the 2D analytic model is calculated compared to the its FEM counterpart. Sensitivity test of Figs. 11 and 12 suggests that the subdomain model is more accurate for analysis of electric machines with thick and shallow depth spoke PMs.

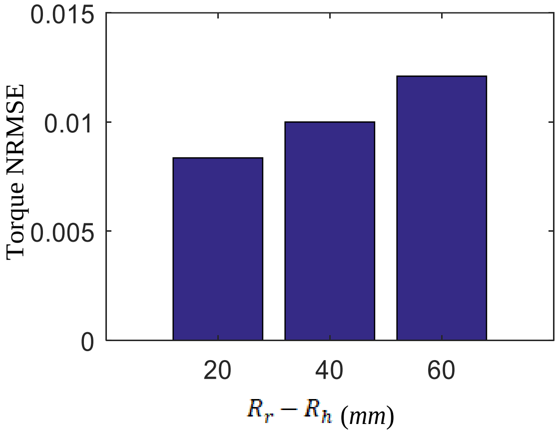

Fig. 11. Torque error variation w.r.t spoke depth change

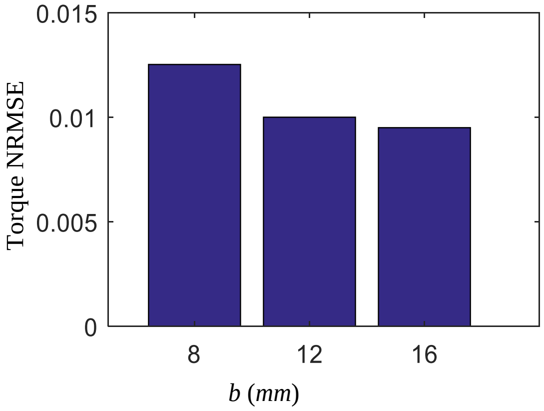

Fig. 12. Torque error variation w.r.t spoke thickness change

13. Conclusion

A two-dimensional analytical assessment of the permanent magnet (PM) and armature reaction (AR) fields in brushless machines utilizing spoke-type PMs has been conducted. The analysis involved the separate calculation of the PM field distribution, armature reaction field, electromagnetic torque, and back electromotive force (back-EMF) using a two-dimensional analytical method. Additionally, the role of the magnet hub in enhancing the PM field, resultant torque, and back-EMF was examined. The results of the analytical calculations were validated through comparison with finite element method (FEM) results, demonstrating that the model provides a high degree of accuracy in predicting the magnetic characteristics of brushless PM machines featuring both arc-shaped and cubic spoke PMs. Moreover, the model revealed to have more accurate results in analysis of electric machines with thick and shallow cubic Spoke PMs.

References

[1] Rahideh, A., & Korakianitis, T. (2013). Analytical calculation of open-circuit magnetic field distribution of slotless brushless PM machines. *International Journal of Electrical Power & Energy Systems*, *44*(1), 99-114.

[2] Yang, Y., Yan, B., Wang, N., & Wang, X. (2016). Analytical prediction of electromagnetic performance of vernier machine with rotor eccentricity. *Electric Power Components and Systems*, *44*(15), 1693-1706.

[3] Ranlöf, M., & Lundin, U. (2009). Finite element analysis of a permanent magnet machine with two contra-rotating rotors. *Electric Power Components and Systems*, *37*(12), 1334-1347.

[4] Rezaeealam, B. (2021). Finite-element/boundary-element transient modelling of hysteresis motors. *Journal of Magnetism and Magnetic Materials*, *519*, 167474.

[5] Wu, Q., Wang, L., Yang, G., & Tang, E. (2022). Structural design and performance prediction of novel modular tubular permanent magnet linear synchronous motor. *Journal of Magnetism and Magnetic Materials*, *564*, 170158.

[6] Yamazaki, K., Fukushima, Y., & Sato, M. (2008, October). Loss analysis of permanent magnet motors with concentrated windings-variation of magnet eddy current loss due to stator and rotor shapes. In *2008 IEEE Industry Applications Society Annual Meeting* (pp. 1-8). IEEE.

[7] Yamazaki, K., & Abe, A. (2009). Loss investigation of interior permanent-magnet motors considering carrier harmonics and magnet eddy currents. *IEEE Transactions on Industry Applications*, *45*(2), 659-665.

[8] Yamazaki, K., & Fukushima, Y. (2011). Effect of eddy-current loss reduction by magnet segmentation in synchronous motors with concentrated windings. *IEEE Transactions on Industry Applications*, *47*(2), 779-788.

[9] El-Refaie, A. M., Alexander, J. P., Galioto, S., Reddy, P. B., Huh, K. K., de Bock, P., & Shen, X. (2014). Advanced high-power-density interior permanent magnet motor for traction

applications. *IEEE Transactions on Industry Applications*, *50*(5), 3235-3248.

[10] Ugale, R. T., Chaudhari, B. N., Baka, S., Dambhare, S. S., & Pramanik, A. (2014). Induced pole rotor structure for line start permanent magnet synchronous motors. *IET Electric Power Applications*, *8*(4), 131-140.

[11] Galioto, S. J., Reddy, P. B., El-Refaie, A. M., & Alexander, J. P. (2014). Effect of magnet types on performance of high-speed spoke interior-permanent-magnet machines designed for traction applications. *IEEE Transactions on Industry Applications*, *51*(3), 2148-2160.

[12] Zhao, W., Lipo, T. A., & Kwon, B. I. (2015). Torque pulsation minimization in spoke-type interior permanent magnet motors with skewing and sinusoidal permanent magnet configurations. *IEEE Transactions on Magnetics*, *51*(11), 1-4.

[13] Zhang, P., Sizov, G. Y., Ionel, D. M., & Demerdash, N. A. (2015). Establishing the relative merits of interior and spoke-type permanent-magnet machines with ferrite or NdFeB through systematic design optimization. *IEEE Transactions on Industry Applications*, *51*(4), 2940-2948.

[14] Tessarolo, A., Mezzarobba, M., & Menis, R. (2015). Modeling, analysis, and testing of a novel spoke-type interior permanent magnet motor with improved flux weakening capability. *IEEE Transactions on Magnetics*, *51*(4), 1-10.

[15] Pourahmadi-Nakhli, M., Rahideh, A., & Mardaneh, M. (2017). Analytical 2-D model of slotted brushless machines with cubic spoke-type permanent magnets. *IEEE Transactions on Energy Conversion*, *33*(1), 373-382.

[16] Zhang, P., Sizov, G. Y., Ionel, D. M., & Demerdash, N. A. (2013, May). Design optimization of spoke-type ferrite magnet machines by combined design of experiments and differential evolution algorithms. In *2013 International Electric Machines & Drives Conference* (pp. 892-898). IEEE.

[17] Hajdinjak, M., & Miljavec, D. (2019). Analytical calculation of the magnetic field distribution in slotless brushless machines with U-shaped interior permanent magnets. *IEEE Transactions on Industrial Electronics*, *67*(8), 6721-6731.

Biography

Meisam Pourahmadi-Nakhli completed his B.Sc. degree in electrical engineering at Shahed University, Tehran, Iran, in 2007, and M.Sc. and Ph.D. degrees in the same field at the Shiraz University and Shiraz University of technology in 2010 and 2018, respectively. He is now an assistant professor in the Department of Electrical and Computer Engineering at the University of Hormozgan.

Hassan Daryanavard received his B.Sc. degree in electrical engineering from Shahid Rajaei University, Tehran, Iran, in 2008, and M.Sc. and Ph.D. degrees in Digital Electronics from the University of Tabriz and Shahid Beheshti University in 2010 and 2015, respectively. He is now an assistant professor in the Department of Electrical and Computer Engineering at the University of Hormozgan.

Masoud Jokar Kouhanjani received a B.S. degree in electrical engineering and an M.S. degree in Power engineering from Shiraz University, Shiraz, Iran, in 2011 and 2014, respectively. He is currently a member of department of technical study in Shiraz Electric Distribution Company, Shiraz, Iran. His research interests include power electronic converters, Electric machinery design and modelling.

Sina Soltani received a B.S. degree in electrical engineering and an M.S. degree in control engineering from Shiraz University, Shiraz, Iran, in 2011 and 2013, respectively., He is currently an Instrumentation Engineer with Honeywell UOP, Rosemont, IL, USA, within the engineering department. His research interests include estimation theory, nonlinear systems and control, adaptive control, signal processing, data mining, and intelligent methods.